5 February 2026

Steric and Electronic Effects Govern Electron Transfer Rates in Pyridinium Electrolytes

Emmanuel Yankson[1], Madison Shaffer[2], Thomas Guarr[2,3], David Hickey[1]

1. Department of Chemical Engineering and Materials Science Michigan State University
2. Jolt Energy Storage Technologies, LLC
3. Bioeconomy Institute Michigan State University

Steric and Electronic Effects Govern Electron Transfer Rates in Pyridinium Electrolytes

Emmanuel Yankson[1], *Madison Shaffer*[2], *Thomas F. Guarr*[2,3], *David P. Hickey*[1]*

[1]Department of Chemical Engineering and Materials Science, Michigan State University, East Lansing, MI 48824, USA.

[2]Jolt Energy Storage Technologies, LLC, Holland, MI 49424, USA.

[3]Michigan State University Bioeconomy Institute, Michigan State University, Holland, MI, 49424, USA.

Keywords: pyridinium electrolyte, electron transfer kinetics, Marcus-Hush-Levich framework, machine learning in electrochemistry, redox flow batteries

Abstract:

N-substituted pyridiniums are promising candidates for electrochemical energy storage applications due to their high solubility and low redox potentials; however, they often exhibit heterogeneous electron transfer (ET) kinetics that are insufficient for high power applications. Rational molecular design to improve ET rates remains challenging because the quantitative relationships between substituent-level structure and heterogeneous ET kinetics are under described for substituted pyridinium systems. While first-principles ET models provide mechanistic descriptors, they do not provide direct mapping of molecular substituents onto kinetic parameters. Here, we combine electrochemical characterization of a series of 2,6-dialkyl-4-arylpyridinium derivatives with supervised machine learning to develop a predictive structure-kinetics model for the heterogeneous ET rate constant (k^0). The resulting model relates k^0 to the percent buried volume of the pyridinium nitrogen atom ($V_{B,N}$) and the Hammett σ_m parameter,

which yielded a strong performance for both the training set (13 compounds, R^2 = 0.85) and external validation set (four compounds R^2 = 0.92, Q^2 = 0.84). Notably, the model accurately predicts k^0 for a 2,6-diethylpyridium derivative that lies outside the structural and kinetic space of the training set. Electrochemical data were further analyzed within the Marcus-Hush-Levich framework to extract mechanistic parameters. Interpreting the machine-learning-derived structural descriptors through this first-principles model identifies outer-sphere reorganization energy (e.g., solvent polarization and ion pairing energy) as the primary contributor to the observed structure-kinetics relationships. By connecting data-driven models with ET theory, this work provides a physically grounded framework for guiding molecular design to tune heterogeneous ET kinetics in organic redox systems.

Introduction

Redox-active organic molecules have attracted growing attention for non-aqueous redox flow battery (NRFB) applications because their modular molecular frameworks allow for systematic tuning of the electrochemical and physicochemical properties.[1,2] Redox flow batteries employ two circulated electrolyte solutions containing redox-active molecules (anolyte and catholyte) which store energy by undergoing reversible reduction and oxidation reactions at the electrode surfaces.[3] The redox potential and solubility of the electrolyte dictate the theoretical energy density of the system,[4] while electron transfer kinetics govern the achievable power density and strongly influence the charge-discharge efficiency.[5] As a result, even redox-active molecules with favorable thermodynamic properties may deliver limited practical performance if charge transfer at the electrode interface is sluggish.

Electron transfer kinetics play a critical role in determining the charge- discharge efficiency of RFBs, as sluggish kinetics require increased overpotentials to sustain charge transfer at the

electrode interface. Operating at elevated overpotentials not only reduces energy efficiency but can also trigger parasitic side reactions that compromise electrolyte stability. For flow batteries operating at current densities of several hundred mA cm^{-2}, an electron transfer rate constant (k^0) on the order of 10^{-2} cm s^{-1} or greater is often cited as desirable to minimize kinetics contribution to overpotential.[5] By comparison, commercial vanadium RFBs exhibit relatively slow kinetics for the V^{2+}/V^{3+} couple, with reported k^0 values in the range of 10^{-5} – 10^{-4} cm s^{-1}.[6,7] Although practical operation has been achieved through electrode optimization and cell engineering, these values highlight the potential benefits of developing redox-active molecules with intrinsically faster electron transfer kinetics. Moreover, despite the growing library of redox-active organic molecules, many exhibit substantially slower kinetics at electrode interfaces. Pyridinium-based molecules, particularly N-substituted 2,6-dimethylpyridinium derivatives, have emerged as promising anolytes for NRFBs due to their relatively low reduction potentials[8] and high solubilities in non-aqueous solvents.[9] Considerable progress has been made in tuning these thermodynamic properties through molecular design; however, like many organic redox species, pyridiniums often display heterogeneous electron transfer kinetics that are insufficient for high-powered operation.

Despite the recognized importance of electron transfer kinetics for redox flow battery performance, there remains limited mechanistic understanding of how molecular structure governs heterogeneous electron transfer rates for redox-active organic molecules. Existing design strategies have largely focused on tuning redox potential and solubility, while kinetic behavior is treated as an empirical outcome rather than a targetable molecular property. Consequently, there remains a need for predictive and interpretable frameworks that directly link molecular structure to electron transfer kinetics at electrode interfaces. Well-established first-principles electron transfer theory identifies key energetic parameters governing charge transfer rates; however, it does not readily

reveal how specific molecular features map onto these parameters. In contrast, recent studies applying machine learning approaches to RFB electrolyte development have demonstrated the potential of data-driven methods to uncover structure-property relationships that are difficult to access through intuition alone.[10–13] Motivated by these contributions, we sought to integrate physically grounded electron transfer theory with supervised machine learning models to elucidate structure-kinetics relationships for pyridinium-based redox-active molecules. By using molecular descriptors informed by electron transfer physics and subsequently interpreting the resulting models within the Marcus-Hush-Levich framework, this strategy provides a pathway to uncover how electronic and steric substituent effects influence reorganization and solvation effects at electrode interfaces.

The Marcus-Hush-Levich model provides a theoretical framework for describing the rate of heterogeneous electron transfer between a dissolved redox species and an electrode surface in terms of three key parameters: the driving force ($\Delta G°$), the reorganization energy (λ), and the electronic coupling matrix element (H_{AB}).[14] Within the non-adiabatic limit, the electron transfer rate constant (k^0) is given by

$$k^0 = \frac{H_{AB}{}^2}{\sqrt{4\pi\lambda k_B T}} exp\left(-\frac{\left(\Delta G^0 + \lambda\right)^2}{4\lambda k_B T}\right) \quad (1)$$

where k_B is the Boltzmann constant, and T is the absolute temperature. The driving force, ΔG^0, represents the free energy difference between the electron donor and acceptor and, for heterogeneous electron transfer processes, is experimentally controlled through the applied electrode potential. The reorganization energy, λ, comprises both inner-sphere (λ_i) and outer sphere (λ_o) contributions. The inner-sphere component reflects intramolecular structural relaxation accompanying electron transfer, while the outer-sphere component accounts for solvent polarization and reorganization dictated by the surrounding environment.[15] Systems characterized

by high reorganization energies exhibit sluggish kinetics, while smaller reorganization energies favor faster charge transfer.

While the Marcus-Hush-Levich formalism provides a rigorous first-principles framework for understanding the energetics governing electron transfer kinetics, it does not directly establish how molecular features (e.g., substituent electronics, steric encumbrance, or solvation environment) map onto the parameters that control the electron transfer rate. In parallel, data-driven and machine learning approaches have emerged as powerful tools for uncovering correlations between molecular structure and electrochemical performance across large chemical spaces;[16–19] however, when applied without physical constraints, such approaches risk identifying relationships for which mechanistic interpretation and generalization is difficult. Therefore, bridging first-principles electron transfer theory with statistically robust and physically interpretable structure-kinetics relationships remains an open challenge in molecular electrochemistry.

Herein, we address this challenge by integrating physically motivated descriptors derived from electron transfer theory with supervised machine learning models to elucidate structure-kinetics relationships for N-substituted 2,6-dimethylpyridinium derivatives in acetonitrile. By utilizing descriptors rooted in Marcus-Hush-Levich theory and subsequently interpreting the resulting model through kinetic analysis and quantum chemical calculations, we develop predictive structure-kinetics relationships that are both statistically robust and mechanistically grounded (**Figure 1**). This combined approach reveals how electronic and steric substituent effects modulate reorganization energy and ion association behavior at the electrode interface while providing actionable design principles for accelerating electron transfer in redox-active organic molecules.

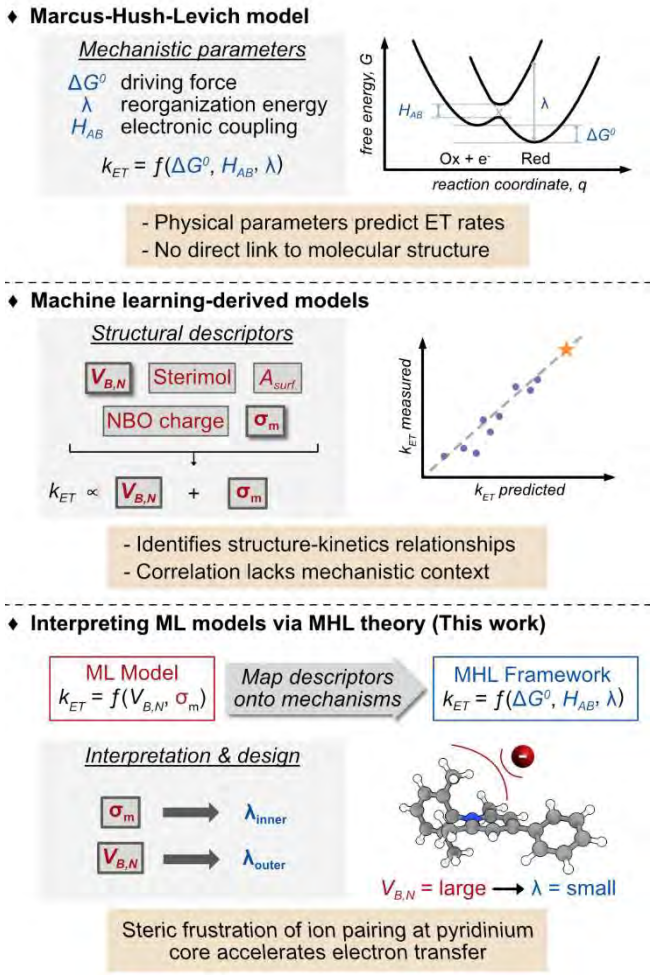

Figure 1. Integrating first-principles electron transfer theory with data-driven modeling to derive molecular design rules for fast heterogeneous electron transfer.

Experimental methods

Materials

The highest available purity was used for all starting materials, which included various amines, Grignard reagents (purchased from Alfa Aesar or Sigma-Aldrich), and 2,6-dimethyl-γ-pyrone (purchased from Ambeed). No additional purification was necessary. Thermo Scientific or Sigma-Aldrich were the sources of the 1 M solutions of arylmagnesium bromides in THF. The anhydrous tetraethylammonium tetrafluoroborate (purity 99.8%) was supplied by MilliporeSigma. Acetonitrile (99.9% extra dry, AcroSeal, molecular sieve-stabilized) was acquired from Acros Organics for use in electrochemical measurements.

General synthetic procedure for 2,6-Dimethylpyridinium compounds

The pyridinium compounds were synthesized following the procedure previously published by Samaroo et al.[9], while the pyrylium intermediates were synthesized using a modified version of the approach reported by DiMauro and Kozlowski.[20,21]

General Synthetic Procedure for 2,6-Dimethylpyrylium Intermediate

In a 250 mL oven-dried round-bottom flask, 2,6-dimethyl-γ-pyrone (30 mmol) was dissolved in 130 mL of THF under a nitrogen atmosphere and cooled to 5 °C using an ice bath. A solution of 1 M arylmagnesium bromide in THF (1 equivalent) was slowly added dropwise to the stirred solution. Over the course of an hour, the reaction was allowed to warm to room temperature after the addition. Boron trifluoride diethyl etherate was then added to the reaction mixture, resulting in the formation of a precipitate. With yields ranging from 40 to 48%, the precipitate was separated by filtration, washed with diethyl ether, and the intermediate pyrylium product was further purified by recrystallization from a 1:1 water/methanol mixture.

General Synthetic Procedure for 2,6-Dimethylpyridinium

The target pyridinium derivatives were synthesized by reacting the corresponding pyrylium intermediate with a primary amine. In a 50 mL round-bottom flask fitted with a magnetic stir bar and condenser, 4-substituted 2,6-dimethyl-pyrylium tetrafluoroborate (9–18 mmol) was suspended in ethanol. Approximately 1.2 equivalents of the primary amine were added, and the mixture was refluxed under a nitrogen atmosphere for 4 hours. After cooling to room temperature overnight, the solution was diluted with diethyl ether. The resulting precipitate was collected by filtration, then dried under vacuum to yield the solid product, with yields ranging from 45% to 68%.

Instrumentation and Electrochemical Characterization

A Biologic VSP multichannel potentiostat was used for cyclic voltammetry experiments, connected to a desktop computer for data collection. The studies used a standard three-electrode setup with platinum wire as the counter electrode, an aqueous Ag/AgCl reference electrode, and a 3 mm rotating glassy carbon disk functioning as the working electrode. The solutions used for the experiments contained 1 mM pyridinium and 100 mM tetraethylammonium tetrafluoroborate in extra-dry acetonitrile (99%) as the supporting electrolyte. The solutions were purged with nitrogen gas for ten minutes prior to each experiment. Every measurement was done at a constant 25 °C temperature.

Determination of Kinetically Controlled Current (i_k)

Rotating disk electrode voltammetry (RDEV) studies were performed with a fixed scan rate of 100 mV s^{-1} for each rotation rate, at 400, 600, 800, and 1000 rotations per minute, to determine the kinetically controlled current. The inverse of the current was plotted against the inverse square root of the corresponding rotation rate (in rad s^{-1}). The resulting linear relationship, consistent with the Koutecky-Levich equation, was used to determine the kinetically controlled current for each pyridinium derivative.

Computational Methods

Gaussian 09 software was used to perform geometry optimizations and density functional theory (DFT) free energy calculations. The B3LYP functional, 6-31+g (d, p) basis set, and CPCM solvation model (acetonitrile) were employed for all computations. Reduction potentials were computed by DFT from the ground state energies of each pyridinium molecule – the oxidized (cation) and reduced (neutral radical). Descriptors for the multivariate regression analysis were derived from the geometry-optimized structures of each pyridinium molecule in their fully

oxidized and reduced states. Percent buried volume ($V_{B,N}$) values were calculated UCSF ChimeraX using Bondi radii, 2.9 A radius around atom centers, and Lebedev integration.[22]

Results & Discussion

Determination of k^0 using Koutecky-Levich Analysis

We initiated our investigation by synthesizing a library of 13 sterically and electronically diverse 2,6-dialkyl-4-arylpyridinium derivatives. This small library of pyridinium structures was designed to probe the relationship between molecular structure and electron transfer kinetics of pyridinium salts at an electrode surface. Pyridinium structures were selected for variation in steric effects of N-substituents (**1** vs **2** vs **9**) and 4-substituents (**5** vs **7**) of the core pyridinium ring. At the N-position, steric hindrance was imparted both by varying the size of the aryl substituent (i.e., **1** vs **2**) and incorporating substituents, such as an N-butyl group, with greater conformational flexibility (**9**). Additionally, compounds **4**, **6**, **10**, and **13** were selected to probe the impact of electronic effects from the N-substituent. It should be noted that there is only a small variation in average molecular radii for the pyridinium cations under investigation; therefore, any differences in electron transfer kinetics can be predominantly attributed to variations in molecular structure. By studying molecules of similar size but variable shape, we aimed to tease out more nuanced relationships between pyridinium structure and electron transfer kinetics.

To measure the electron transfer kinetics of the pyridinium salts studied here, we employed rotating disk electrode voltammetry (RDEV). This technique enables the quantification of the heterogeneous electron transfer rate constant *(k^0)*, which describes the rate of electron transfer between an electroactive species and an electrode surface. Koutecky-Levich analysis of RDEV experiments has been extensively utilized for measuring k^0 of small molecules using Equation 2,[23,24]

(2) $$\frac{1}{i_{obs}} = \frac{1}{i_k} + \frac{1}{i_l} = \frac{1}{i_k} + \frac{1}{0.62nFD_2^{2/3}A\omega^{1/2}v^{-1/6}C_0^*}$$

where n is the number of electrons transferred, F is the Faraday constant, D is the pyridinium diffusivity, A is the electrode area, ν is the kinematic viscosity, and C_0^* is bulk pyridinium concentration. By plotting the inverse of the measured current (i_{obs}) against the inverse square root of the electrode rotation rate (ω), the mass transport limiting current (i_l) and kinetically controlled current (i_k) can be determined by Equation 3. The kinetically controlled current reflects the observed current when mass transfer of pyridinium to the electrode is sufficient to maintain a surface concentration equal to that of the bulk solution. The standard rate constant of pyridiniums were then calculated using Equation 4,

(3) $$i_k = FAk_f(E)C_0^*$$

(4) $$k_f(E) = k^o e^{-\alpha\left(\frac{nF}{RT}\right)(E-E^{0\prime})}$$

where $k_f(E)$ is the potential-dependent rate constant, α is the charge transfer coefficient, R is the gas constant, T is the absolute temperature, E is the applied electrode potential, and $E^{0\prime}$ is the formal pyridinium redox potential. From Equation 4, a linear fit of ln(k_f) versus overpotential (η) gives a straight line, with the y-intercept providing ln(k^0).

Representative RDE voltammograms, the Koutecky-Levich plot, and plot of ln(k_f) versus η for **4** are shown in **Figure 2** (similar plots for all compounds are included in the Supporting Information). From this analysis, the standard electron transfer rate constant was found to be 0.012 ± 0.001 cm s^{-1}. Across the full compound library, k^o values ranged from 0.008 cm s^{-1} to 0.02 cm s^{-1}, with standard deviations less than 5%. Because k^0 values for all pyridiniums in the initial library are on the order of 10^{-2} cm s^{-1}, even modest differences in electron kinetics are likely to be significant in energy storage applications. Consequently, identifying structure-activity relationships is imperative for designing species that can be charged and discharged efficiently.

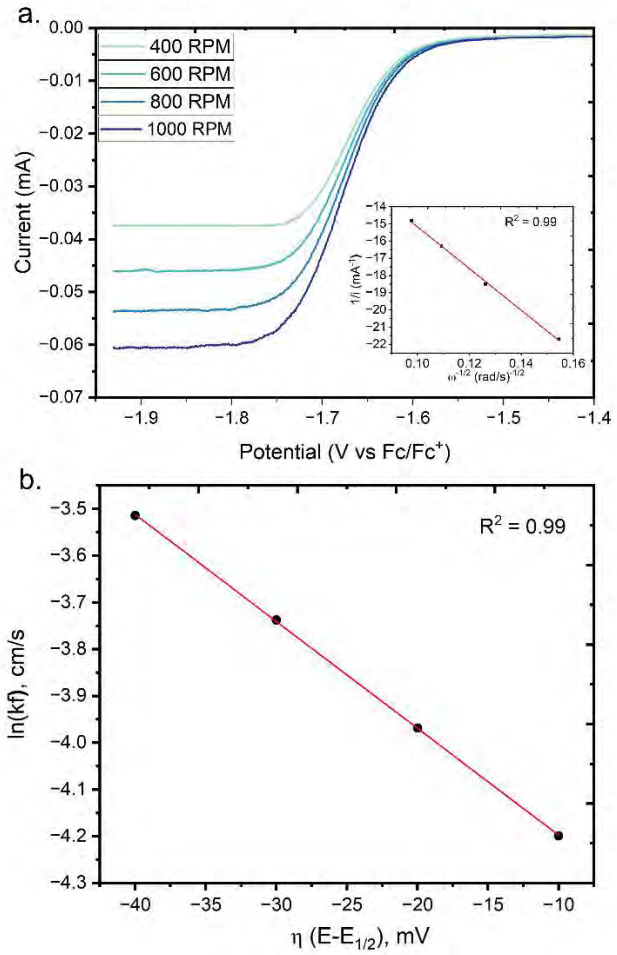

Figure 2. Rotating disc electrode voltammetry (RDEV) characterization of 1 mM N-phenyl-4-p-methoxyphenyl-2,6-dimethyl pyridinium BF_4. (a) Representative RDEV at variable electrode rotation rates with a plot of resulting inverse current versus the inverse square root of rotation rate (inset), and (b) linear fit of ln(k_f) versus overpotential (η). Experiments were performed with a 3 mm glassy carbon RDE in acetonitrile with 0.1M $TEABF_4$ at a scan rate of 100 mV s^{-1} and 25 °C.

From the initial library of pyridiniums (**Figure 3**), several general trends can be observed between structural features and the corresponding electron transfer rate constants. Pyridinium derivatives with a flexible butyl chain at the N-position (**9** and **10**) exhibit significantly slower k^o compared to analogous pyridiniums with a rigid aromatic ring as the N-substituent (**1** and **4**, respectively). In contrast, compounds with identical N-substituents but different substituents at the 4-position show substantial variation in k^0. For example, the N-mesityl derivative containing a 4-phenyl substituent (**2**) exhibits a k^0 nearly double that of the derivative with a 4-(p-tolyl) substituent (**8**) (0.015 ± 0.001 versus 0.008 ± 0.001 cm s^{-1}). On the other hand, comparisons of **3** and **8** (0.008

± 0.001 cm s^{-1} for both), as well as **2** and **7** (0.015 ± 0.001 and 0.015 ± 0.001 cm s^{-1}, respectively) suggest that certain N-substituent changes exert minimal effect. In the case of 4-methoxyphenyl derivatives with N-mesityl (**6**) and N-phenyl (**4**), there is no significant difference in their corresponding k^0 (0.012 ± 0.002 versus 0.012 ± 0.001 cm s^{-1}, respectively). While these results suggest that both the N-substituent and the 4-substituent can influence electron transfer kinetics, the effect is highly context-dependent. In many cases, subtle electronic or steric changes at the 4-position result in meaningful differences in k^0.

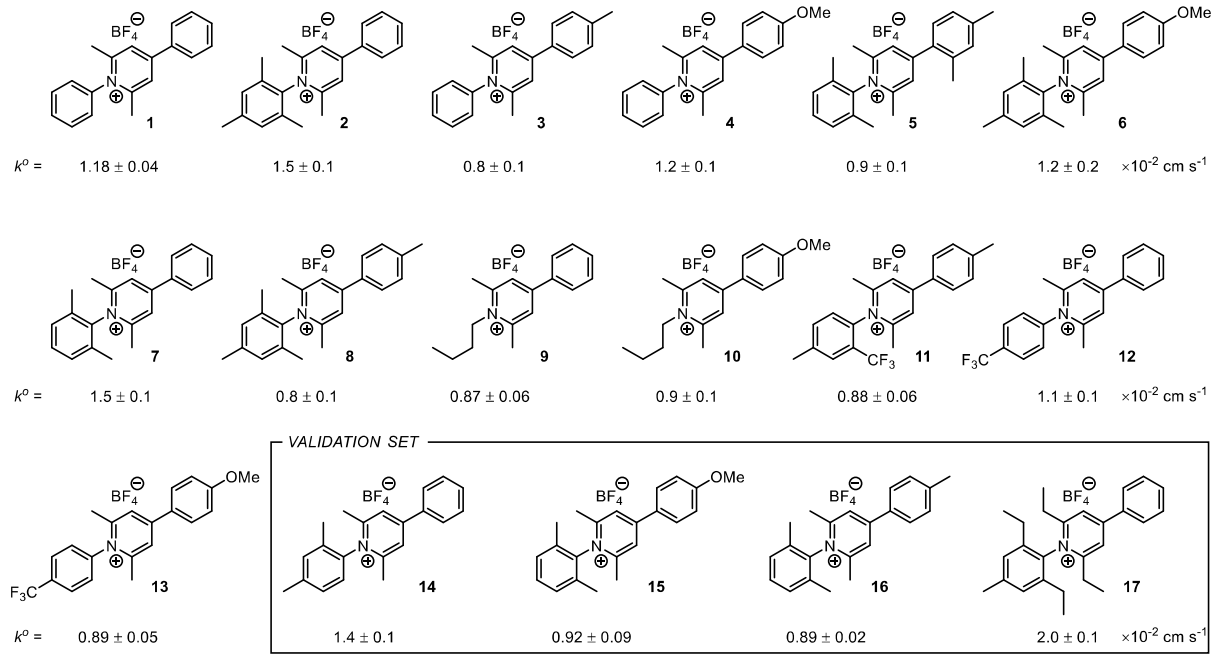

Figure 3. Structure and corresponding electron transfer rate constants (k^0) of pyridinium molecules in this study.

Compton and co-workers have systematically investigated the relationship between molecular size and the corresponding heterogeneous electron transfer rate constant for substituted anthracene, quinone, and ferrocene derivatives.[25] Specifically they identified a non-monotonic relationship between the measured k^0 of a molecule and its corresponding solvodynamic radius (r_s) with a localized maximum at $r_s \approx 0.5$ nm.[26] The solvodynamic radius of a solution-phase species provides a more realistic measure of the solvated molecular radius than crystallographic

radii, and the effective solvodynamic radius can be readily estimated from diffusivity (D) using the Stokes-Einstein equation,

(5) $$r_s = \frac{k_B T}{6\pi\eta D}$$

where, k_B is the Boltzmann constant, T is the absolute temperature, η is the solution viscosity, and D is the diffusivity of the redox species. A plot of k^0 as a function of r_s for pyridiniums studied in this work is shown in **Figure 4**, where r_s values were derived from previously reported diffusivities.[27] A theoretical relationship between k_0 and r_s (**Figure 4**, dashed line) was generated using a simplified model in which r_s serves as the primary descriptor of molecular structure. In contrast to the strong correlation previously observed for substituted anthracene derivatives, no analogous trend was identified for 2,6-dimethylpyridiniums. This divergence may reflect the greater steric variation in pyridinium substituents, the cationic nature of redox-active core, or differences in ion-pairing and interfacial solvation behavior. Together, these observations highlight the limitations of single-parameter descriptors and underscore the need for a more systematic approach to elucidate structure-kinetic relationships in heterogeneous electron transfer.

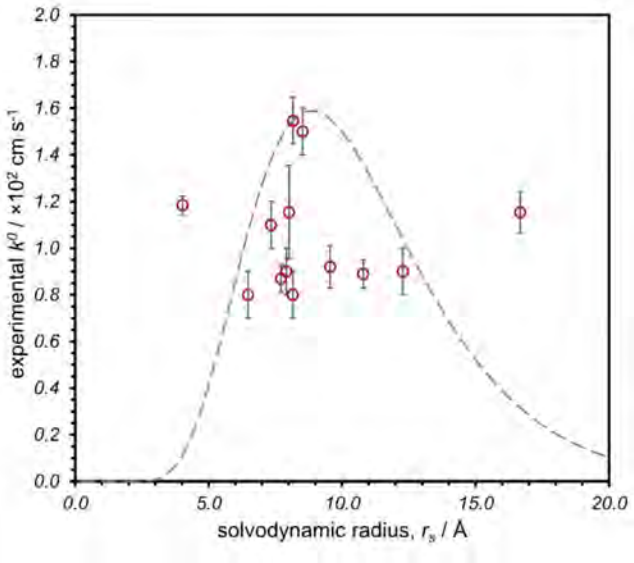

Figure 4. A plot of experimentally determined heterogeneous electron transfer rate constants (k^0) versus solvodynamic radius(r_s) for all pyridiniums studied. Rate constants are reported as the mean value ± one standard deviation (n = 3). The theoretical relationship between k^0 and r_s for the pyridiniums studied based on a simplified Marcus framework.[26] Rate constants and radii were calculated from experiments performed using 0.1 M TEA BF_4 in acetonitrile at 25 °C.

Computational approach to understanding kinetic behavior of pyridinium molecules

To better understand the relationship between electrode kinetics and pyridinium structure, we employed a supervised machine learning approach[28]. This method uses regression analysis to identify linear combinations of molecular descriptors (independent variables) that correlate with the experimentally measured electron transfer rate constants (dependent variables). Molecular descriptors were extracted from Density Functional Theory (DFT) computations of geometry optimized pyridinium derivatives. To validate the computed pyridinium structures, we compared experimentally measured one-electron reduction potentials with those derived from DFT calculations (**Figure 5**). The strong linear correlation between the measured and calculated redox potentials (R^2 = 0.89) supports the accuracy of the optimized geometries and the derived modelled parameters. A full description of the procedure used to calculate E^o from DFT computations is included in the Supporting Information.

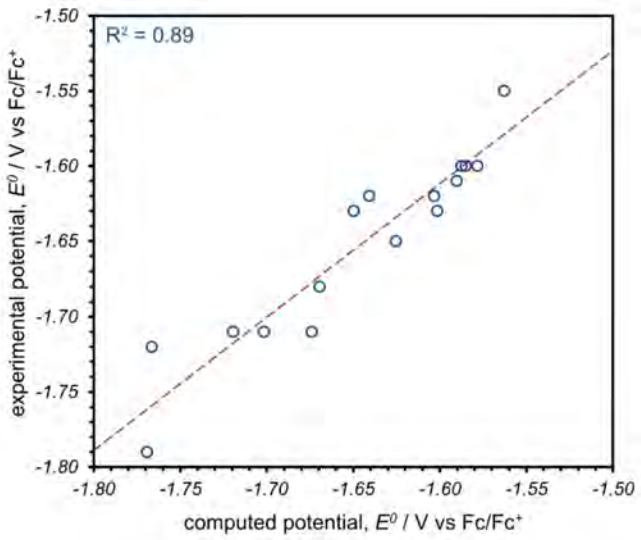

Figure 5. A plot of experimentally measured redox potentials for all pyridiniums studied versus the corresponding DFT computed potentials (both versus a ferrocene/ferrocenium reference potential). Computed potentials were

calculated from geometry-optimized ground state pyridinium structures using the CPCM solvation model with acetonitrile as the solvent. Experimental potentials were calculated from CV data using 0.1 M TEA BF_4 in acetonitrile at 25 °C.

Statistical Model Development and Validation

A key advantage of supervised machine learning is the capacity to evaluate mechanistic hypotheses through the deliberate selection of physically meaningful descriptors; this allows the presence or absence of predictive correlations to be assessed quantitatively. Descriptor selection for this work was guided by the Marcus-Hush-Levich framework for electron transfer, which emphasizes the role of reorganization energy in governing electron transfer kinetics. Accordingly, we focused on parameters expected to influence both solvent and inner-sphere reorganization energies. Both electronic descriptors (*e.g.*, Hammett sigma parameters, NBO charges) and steric descriptors (*e.g.*, Sterimol parameters, surface area) were considered to probe structure-kinetics relationships, and all descriptors were scaled using Z-score normalization. Subsequent multiple linear regression analysis resulted in a parsimonious model comprising two descriptors (**Figure 6**): the Hammett meta substituent constant (σ_m) for the 4-aryl group and the percent buried volume of the pyridinium nitrogen atom ($\%V_{B,N}$). The resulting model revealed a strong correlation between these parameters and k^0 (R^2 = 0.85, Q^2 = 0.84),

(6) $$k^0 = 0.71\sigma_m + 0.44\%V_{B,N} + 0.48\sigma_m\%V_{B,N}$$

In the context of this model, σ_m describes the through-field inductive electronic influence of the 4-substituent, while $\%V_{B,N}$ quantifies the degree of steric encumbrance surrounding the redox-active nitrogen center. The positive coefficients associated with both σ_m and $\%V_{B,N}$ suggests that faster electron transfer kinetics are associated with pyridinium derivatives bearing inductively electron-withdrawing substituents and increased steric shielding proximal to the pyridinium core. These correlations are consistent with a reduction in reorganization energy and/or disruption of unfavorable solvation or ion pairing interactions at the electrode interface. Notably, increased

steric encumbrance at the nitrogen center may also frustrate tight ion pairing or ordered interfacial solvation, which would lower the activation barrier for electron transfer.

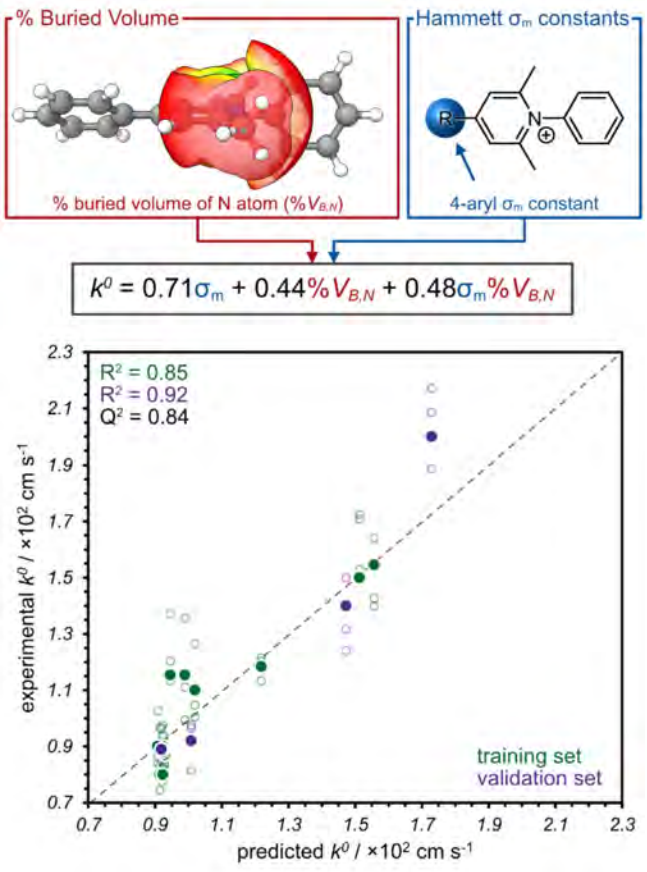

Figure 6. (Top) Visual depictions of the percent buried volume ($\%V_{B,N}$) and Hammett (σ_m) parameters used to model the electron transfer rate constant of 2,6-dimethylpyridiniums (k^0). (Bottom) Plot of experimental and predicted k^0 values, where the solid circles represent the mean experimental rate constants (n = 3) and the hollow circles depict the individual measurements for all compounds.

Using the σ_m and $\%V_{B,N}$ descriptors identified in the regression model, an independent external validation was performed by predicting k^0 for four additional pyridinium derivatives. Validation species were selected to span a range of predicted k^0 values to serve as interpolation (**14-16**) and extrapolation (**17**) within the chemical space defined by the training set. Across the validation set, predicted k^0 values showed excellent agreement with experimental data: **14** (k^0_{pred} = 0.014 cm s^{-1}, k^0_{meas} = 0.014 ± 0.001 cm s^{-1}), **15** (k^0_{pred} = 0.010 cm s^{-1}, k^0_{meas} = 0.0090 ± 0.0009 cm s^{-1}), **16** (k^0_{pred} = 0.009 cm s^{-1}, k^0_{meas} = 0.0090 ± 0.0002 cm s^{-1}), and **17** (k^0_{pred} = 0.017 cm s^{-1},

k^0_{meas} = 0.020 ± 0.001 cm s^{-1}). Notably, **17** represents an expansion of the core pyridinium framework with ethyl substituents at C2 and C6 on both the pyridinium and N-substituent rings, which result in a high percent buried volume of the nitrogen atom (86%). Despite this structural divergence, the model accurately predicts its electron transfer kinetics.

The strong predictive performance of the model suggests that the selected descriptors capture key structural factors governing heterogeneous electron transfer kinetics, which are commonly interpreted in terms of contributions to the total reorganization energy. These correlations may arise from multiple non-exclusive mechanisms. A positive correlation between σ_m and k^0 is consistent with reduced electron density on the pyridinium ring, which may lower inner-sphere reorganization energy. In parallel, positive correlations between steric encumbrance at the nitrogen center and k^0 may reflect weaker counterion association and diminished solvent reorganization penalties at the electrode interface. To further evaluate the contribution of inner sphere reorganization energy to these trends, DFT computations were performed to quantify molecular reorganization energies for the pyridinium derivatives examined.

Theoretical calculation of Reorganization Energy Involved in the Electron Transfer Process

The total reorganization energy associated with heterogeneous electron transfer can be estimated from experimentally measured k^0 values following the approach outlined by Constentin and coworkers.[29] Using this approach, the forward heterogeneous electron transfer rate constant, (k_f) is expressed as:

(7) $$k_f = Zexp\left(-\frac{\Delta G_f^{\neq}}{RT}\right)$$

where Z is a pre-exponential factor related to the electronic coupling and nuclear dynamics of the electron transfer process, R is the gas constant, T is the absolute temperature, and $\Delta G^{\neq}_f$ is the

activation energy barrier for electron transfer at the electrode. The activation free energy is related to the reorganization energy by the Marcus expression,

(8) $$\Delta G_f^{\neq} = \frac{\lambda}{4}\left(1 + \frac{\Delta G^0}{\lambda}\right)^2$$

where ΔG^0 is the driving force of the electron transfer reaction, which is related to the applied electrode potential (E_{app}) and the standard redox potential (E^0) by

(9) $$\Delta G^0 = -nF(E_{app} - E^0)$$

where n is the number of electrons transferred (here, n = 1), and F is Faraday's constant. Importantly, the standard electron transfer rate constant (k^0) is equivalent to the k_f under zero driving force (i.e., $E_{app} = E^0$ and $\Delta G^0 = 0$). For non-adiabatic electron transfers, the pre-exponential factor (Z) can be reasonably approximated by the molecular collisional frequency,

(10) $$Z = \sqrt{\frac{RT}{2\pi M}}$$

where M is the combined molecular weight of the redox species and its associated counterion. To assess the validity of this approximation, variable temperature rotating disk voltammetry experiments were performed using **1** as a representative species (experimental determination of Z is provided in the Supporting Information). These measurements yielded an experimental pre-exponential factor of Z = 4000 cm s^{-1}, which is in close agreement with the collisional frequency estimate (Z = 3370 cm s^{-1}). This agreement supports the assumption that the electron transfer in this system is consistent with non-adiabatic behavior. Accordingly, collisional frequency estimates were employed to approximate pre-exponential factors for all pyridinium derivatives, thus enabling calculation of total reorganization energies. The resulting λ_{total} values fall within a narrow range of 1.22 – 1.33 eV (**Figure 7b**). While explicit determination of the solvent reorganization energy requires detailed atomistic simulations, its contribution may be inferred by comparing λ_{total}

to inner sphere reorganization energy (λ_{inner}), which can be computed using well-established quantum chemical methods. Differences between λ_{inner} and λ_{total} may therefore reflect substituent-dependent variations in solvent reorganization and counterion dynamics at the electrode interface.

Inner sphere reorganization energies were calculated using the direct method described by Rosso *et al.*[30] Density functional theory (DFT) computations were performed using the B3LYP functional with the 6-31+g (d, p) basis set and CPCM implicit solvation model. For each pyridinium, geometry optimizations were carried out for both the oxidized state (Py^+) and the reduced state (Py^*). The energy of the reduced species evaluated at the oxidized-state geometry corresponds to the diabatic charge-transfer state.[31] The inner sphere reorganization energy was then computed according to,

(11) $$\lambda_i = G_{Py^*}(Py^+) - G_{Py^+}(Py^+)$$

where $G_{Py+}(Py^+)$ is the ground-state energy of the oxidized species at its optimized geometry, and $G_{Py*}(Py^+)$ is the energy of the reduced species evaluated at the oxidized geometry (**Figure 7a**). The fractional contribution of λ_{inner} to λ_{total} was calculated by

(12) $$\%\lambda_{inner} = \frac{\lambda_{inner}}{\lambda_{total}} \times 100\%$$

Across the pyridinium series examined, inner sphere reorganization energy accounts for approximately 13 – 21% of the total reorganization energy (**Figure 7b**). This result suggests that solvent and outer-sphere contributions dominate the overall reorganization energy landscape for heterogeneous electron transfer kinetics in pyridinium-based systems. This is consistent with the strong sensitivity of electron transfer kinetics to substituent-dependent solvation and ion-pairing effects. The relatively small contribution of λ_{inner} further supports the relevance of steric and electronic descriptors that primarily modulate solvent reorganization and counterion dynamics.

A.

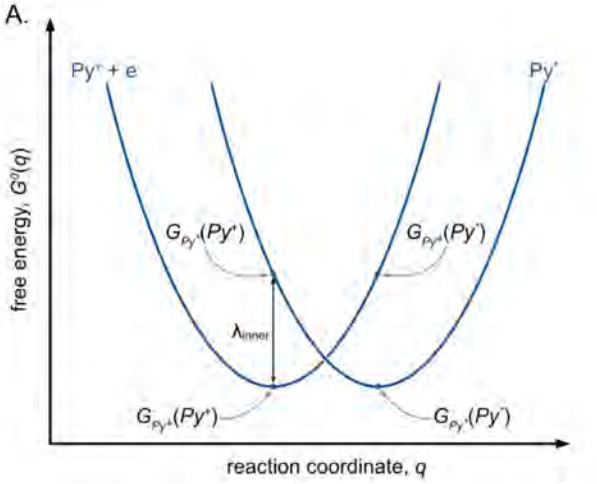

B.

Compound	λ_{total} (eV)	λ_{inner} (eV)	$\%\lambda_{inner}$ ($100*\lambda_{inner}/\lambda_{total}$)
1	1.29	0.183	14.2
2	1.26	0.204	16.2
3	1.33	0.181	13.6
4	1.29	0.185	14.3
5	1.31	0.212	16.2
6	1.28	0.164	12.8
7	1.26	0.195	15.4
8	1.32	0.213	16.1
9	1.33	0.190	14.3
10	1.32	0.223	16.9
11	1.31	0.224	17.1
12	1.29	0.257	19.9
13	1.31	0.269	20.6
14	1.27	0.172	13.5
15	1.31	0.148	11.3
16	1.31	0.185	14.1
17	1.22	-	-

Figure 7. (A) Gibbs free energy curves as a function of the reaction coordinate for electron transfer according to the Marcus-Hush-Chidsey model for the reduction of pyridinium (Py^+) to pyridine radical (Py^*). Coordinates used for the calculation of inner sphere reorganization energy are highlighted.[32,31] $G_a(b)$ represents the energy of oxidation state a at the constrained geometry of state b. (B) Table summarizing the calculated reorganization energies for each pyridinium. Fractional contribution of inner-sphere reorganization energy given as $100\% * \lambda_{inner} / \lambda_{total}$.

Physical Significance of the Electron Transfer Kinetic Model

We next consider how the steric encumbrance at the pyridinium nitrogen influences the reorganization energy associated with heterogeneous electron transfer. The percent buried volume provides a quantitative measure of the extent to which the redox-active nitrogen center is sterically shielded by its local molecular environment. The observed positive correlation between buried volume and heterogeneous electron transfer rate suggests that increased steric shielding is associated with faster electron transfer kinetics. This trend may be consistent with a model in which buried volume modulates the strength of ion pairing between the oxidized pyridinium cation and its counterion. For pyridiniums with low buried volume, the nitrogen atom is more exposed in the oxidized state and thus more prone to strong ion pairing. Upon reduction, the neutral product weakens or disrupts these interactions, which requires substantial solvent and counterion reorganization. The accompanying reorganization penalty contributes to a larger solvent reorganization energy and, consequently, slower electron transfer kinetics. In contrast, increased steric shielding around the nitrogen center may weaken ion-pairing in the oxidized state,

potentially reducing the extent of structural and solvent rearrangement required upon electron transfer. Diminished solvent reorganization associated with this transition would lower the activation barrier for electron transfer, thereby leading to enhanced kinetics. Together, these observations suggest that steric modulation of the pyridinium nitrogen may play a role in influencing solvent reorganization and ion pairing contributions to the overall reorganization energy.

It should be noted that, while the formal positive charge resides on the nitrogen atom, the electrostatic potential of a pyridinium cation is distributed over the ring's π framework; consequently, counterion association does not need to be localized to the nitrogen atom but can occur over the accessible ring face and perimeter.[33] In this context, $V_{B,N}$ can be interpreted as a geometric proxy for the accessibility of the cationic pyridinium surface and the range of available ion pair geometries. Increased steric encumbrance around the nitrogen center restricts close counterion approach to the pyridinium π system. This favors more solvent-separated ion association and reduces the extent of solvent and counterion reorganization required upon reduction, thereby accelerating electron transfer.

Conclusion

In this work, we demonstrate that heterogeneous electron transfer kinetics in 2,6-dialkyl-4-arylpyridinium-based species cannot be rationalized solely in terms of molecular size or diffusivity, but rather emerge from a combination of electronic structure, steric environment, and solvation dynamics. Supervised machine learning was used to develop a predictive statistical model relating experimentally measured heterogeneous electron transfer rate constants of 2,6-dialkyl-4-arylpyridinium derivatives to two physically interpretable descriptors, an inductive electronic parameter (σ_m) and a steric parameter quantifying the buried volume of the pyridinium

nitrogen ($V_{B,N}$). The resulting model accurately predicted experimentally measured rate constants across both training and validation sets and was used to guide the design of a new pyridinium (**17**) that is an extrapolation of the original data set and exhibits a rate constant of 0.02 cm s^{-1} (twice the minimum threshold of 0.01 cm s^{-1} recommended for efficient RFB operation). Analysis of reorganization energies reveals that inner sphere contributions are relatively minor, while solvent and outer sphere effects dominate the activation barrier to electron transfer. These results are consistent with a mechanistic picture in which steric encumbrance influences ion association and solvent organization around the delocalized cationic surface of the pyridinium ring, while modulating the amount of solvent reorganization required upon electrochemical reduction. Molecular designs that sterically frustrate ion pairing at the pyridinium nitrogen may minimize solvent reorganization penalties and enable faster heterogeneous electron transfer kinetics. This work illustrates how the framework of utilizing physically grounded molecular descriptors in combination with data-driven modeling can provide deeper insight into actionable molecular-level design principles for redox-active species in energy storage systems.

ASSOCIATED CONTENT

Supporting Information. The supporting information is available free of charge.

AUTHOR INFORMATION

Corresponding Author

***David P. Hickey – hickeyd6@msu.edu**

Author Contributions

E.Y., T.F.G. and D.P.H. were responsible for the conceptualization of the project. E.Y. and M.S. performed all synthetic procedures. E.Y. performed all electrochemical measurements and calculations. E.Y. and D.P.H. prepared the Supporting Information. E.Y. and D.P.H. drafted the

original version of the manuscript. All authors contributed to reviewing and editing the final manuscript. The manuscript was written through contributions of all authors. All authors have given approval to the final version of the manuscript.

ACKNOWLEDGMENT

This work was partially funded by Jolt Energy Storage Technology, LLC. We thank Dr. S. Barton for allowing us access to his lab for RDE experiments. Computational resources were provided by the High-Performance Computing Cluster (HPCC) at Michigan State University.

References

(1) Leung, P.; Shah, A. A.; Sanz, L.; Flox, C.; Morante, J. R.; Xu, Q.; Mohamed, M. R.; Ponce de León, C.; Walsh, F. C. Recent Developments in Organic Redox Flow Batteries: A Critical Review. *Journal of Power Sources*. Elsevier B.V. 2017, pp 243–283. https://doi.org/10.1016/j.jpowsour.2017.05.057.

(2) Chen, H.; Cong, G.; Lu, Y. C. Recent Progress in Organic Redox Flow Batteries: Active Materials, Electrolytes and Membranes. *Journal of Energy Chemistry*. Elsevier B.V. September 1, 2018, pp 1304–1325. https://doi.org/10.1016/j.jechem.2018.02.009.

(3) Chalamala, B. R.; Soundappan, T.; Fisher, G. R.; Anstey, M. R.; Viswanathan, V. V.; Perry, M. L. Redox Flow Batteries: An Engineering Perspective. *Proceedings of the IEEE* **2014**, *102* (6), 976–999. https://doi.org/10.1109/JPROC.2014.2320317.

(4) Olabi, A. G.; Allam, M. A.; Abdelkareem, M. A.; Deepa, T. D.; Alami, A. H.; Abbas, Q.; Alkhalidi, A.; Sayed, E. T. Redox Flow Batteries: Recent Development in Main Components, Emerging Technologies, Diagnostic Techniques, Large-Scale Applications, and Challenges and Barriers. *Batteries*. Multidisciplinary Digital Publishing Institute (MDPI) August 1, 2023. https://doi.org/10.3390/batteries9080409.

(5) Sawant, T. V.; Yim, C. S.; Henry, T. J.; Miller, D. M.; McKone, J. R. Harnessing Interfacial Electron Transfer in Redox Flow Batteries. *Joule*. Cell Press February 17, 2021, pp 360–378. https://doi.org/10.1016/j.joule.2020.11.022.

(6) Yamamura, T.; Watanabe, N.; Yano, T.; Shiokawa, Y. Electron-Transfer Kinetics of Np[Sup 3+]/Np[Sup 4+], NpO[Sub 2][Sup +]/NpO[Sub 2][Sup 2+], V[Sup 2+]/V[Sup 3+], and VO[Sup 2+]/VO[Sub 2][Sup +] at Carbon Electrodes. *J. Electrochem. Soc.* **2005**, *152* (4), A830. https://doi.org/10.1149/1.1870794.

(7) Sum, E.; Skyllas-Kazacos, M. A Study of the V(II)/V(III) Redox Couple for Redox Flow Cell Applications. *J. Power Sources* **1985**, *15* (2–3), 179–190. https://doi.org/10.1016/0378-7753(85)80071-9.

(8) Samaroo, S.; Pattillo, A. L.; Servinski, D.; Kruper, W. R.; Carter, D. D.; Guarr, T. F.; Hickey, D. P. Low Viscosity, High Concentration Pyridinium Anolytes for Organic Nonaqueous Redox Flow Batteries. *ACS Applied Energy Materials*. American Chemical Society 2023. https://doi.org/10.1021/acsaem.3c02370.

(9) Samaroo, S.; Hengesbach, C.; Bruggeman, C.; Carducci, N. G. G.; Mtemeri, L.; Staples, R. J.; Guarr, T.; Hickey, D. P. C–H···π Interactions Disrupt Electrostatic Interactions between Non-Aqueous Electrolytes to Increase Solubility. *Nat. Chem.* **2023**, *15* (10), 1365–1373. https://doi.org/10.1038/s41557-023-01291-1.

(10) Yan, Y.; Robinson, S. G.; Sigman, M. S.; Sanford, M. S. Mechanism-Based Design of a High-Potential Catholyte Enables a 3.2 V All-Organic Nonaqueous Redox Flow Battery. *J. Am. Chem. Soc.* **2019**, *141* (38), 15301–15306. https://doi.org/10.1021/jacs.9b07345.

(11) Robinson, S. G.; Yan, Y.; Hendriks, K. H.; Sanford, M. S.; Sigman, M. S. Developing a Predictive Solubility Model for Monomeric and Oligomeric Cyclopropenium-Based Flow Battery Catholytes. *J. Am. Chem. Soc.* **2019**, *141* (26), 10171–10176. https://doi.org/10.1021/jacs.9b04270.

(12) Sevov, C. S.; Hickey, D. P.; Cook, M. E.; Robinson, S. G.; Barnett, S.; Minteer, S. D.; Sigman, M. S.; Sanford, M. S. Physical Organic Approach to Persistent, Cyclable, Low-Potential Electrolytes for Flow Battery Applications. *J. Am. Chem. Soc.* **2017**, *139* (8), 2924–2927. https://doi.org/10.1021/jacs.7b00147.

(13) Kim, S.; Jinich, A.; Aspuru-Guzik, A. MultiDK: A Multiple Descriptor Multiple Kernel Approach for Molecular Discovery and Its Application to Organic Flow Battery Electrolytes. *J. Chem. Inf. Model.* **2017**, *57* (4), 657–668. https://doi.org/10.1021/acs.jcim.6b00332.

(14) Marcus, R. A.; Sutin, N. Electron Transfers in Chemistry and Biology. *Biochimica et Biophysica Acta (BBA) - Reviews on Bioenergetics* **1985**, *811* (3), 265–322. https://doi.org/10.1016/0304-4173(85)90014-X.

(15) Bard, A. J.; Faulkner, L. R.; White, H. S. *Electrochemical Methods: Fundamentals and Applications*, 3rd ed.; John Wiley & Sons, Ltd.: Oxford, 2022.

(16) Zhong, P.; Deng, B.; He, T.; Lun, Z.; Ceder, G. Deep Learning of Experimental Electrochemistry for Battery Cathodes across Diverse Compositions. *Joule* **2024**, *8* (6), 1837–1854. https://doi.org/10.1016/j.joule.2024.03.010.

(17) Zheng, Z.; Florit, F.; Jin, B.; Wu, H.; Li, S.; Nandiwale, K. Y.; Salazar, C. A.; Mustakis, J. G.; Green, W. H.; Jensen, K. F. Integrating Machine Learning and Large Language Models to Advance Exploration of Electrochemical Reactions. *Angewandte Chemie International Edition* **2025**, *64* (6), e202418074. https://doi.org/10.1002/anie.202418074.

(18) Mistry, A.; Franco, A. A.; Cooper, S. J.; Roberts, S. A.; Viswanathan, V. How Machine Learning Will Revolutionize Electrochemical Sciences. *ACS Energy Lett.* **2021**, *6* (4), 1422–1431. https://doi.org/10.1021/acsenergylett.1c00194.

(19) Robinson, S. G.; Sigman, M. S. Integrating Electrochemical and Statistical Analysis Tools for Molecular Design and Mechanistic Understanding. *Acc. Chem. Res.* **2020**, *53* (2), 289–299. https://doi.org/10.1021/acs.accounts.9b00527.

(20) Yue, H.; Zhu, C.; Shen, L.; Geng, Q.; Hock, K. J.; Yuan, T.; Cavallo, L.; Rueping, M. Nickel-Catalyzed C-N Bond Activation: Activated Primary Amines as Alkylating Reagents in Reductive Cross-Coupling. *Chem. Sci.* **2019**, *10* (16), 4430–4435. https://doi.org/10.1039/c9sc00783k.

(21) DiMauro, E. F.; Kozlowski, M. C. Phosphabenzenes as Electron Withdrawing Phosphine Ligands in Catalysis. *J. Chem. Soc. Perkin 1.* **2002**, *2* (3), 439–444. https://doi.org/10.1039/b101454o.

(22) Meng, E. C.; Goddard, T. D.; Pettersen, E. F.; Couch, G. S.; Pearson, Z. J.; Morris, J. H.; Ferrin, T. E. <scp>UCSF ChimeraX</Scp> : Tools for Structure Building and Analysis. *Protein Science* **2023**, *32* (11), e4792. https://doi.org/10.1002/pro.4792.

(23) Laoire, C. O.; Plichta, E.; Hendrickson, M.; Mukerjee, S.; Abraham, K. M. Electrochemical Studies of Ferrocene in a Lithium Ion Conducting Organic Carbonate Electrolyte. *Electrochim. Acta* **2009**, *54* (26), 6560–6564. https://doi.org/10.1016/j.electacta.2009.06.041.

(24) Crawley, C. D.; Hawkridge, F. M. Rotating Disk Electrode Voltammetric Determination of the Heterogeneous Electron Transfer Kinetics of Soluble Spinach Ferredoxin. *J. Electroanal. Chem. Interfacial Electrochem.* **1983**, *159* (2), 313–324. https://doi.org/10.1016/S0022-0728(83)80630-5.

(25) Henstridge, M. C.; Laborda, E.; Rees, N. V.; Compton, R. G. Marcus–Hush–Chidsey Theory of Electron Transfer Applied to Voltammetry: A Review. *Electrochim. Acta* **2012**, *84*, 12–20. https://doi.org/10.1016/j.electacta.2011.10.026.

(26) Clegg, A. D.; Rees, N. V.; Klymenko, O. V.; Coles, B. A.; Compton, R. G. Marcus Theory of Outer-Sphere Heterogeneous Electron Transfer Reactions: Dependence of the Standard Electrochemical Rate Constant on the Hydrodynamic Radius from High Precision Measurements of the Oxidation of Anthracene and Its Derivatives in Nonaqueous Solvents Using the High-Speed Channel Electrode. *J. Am. Chem. Soc.* **2004**, *126* (19), 6185–6192. https://doi.org/10.1021/ja040014v.

(27) Samaroo, S.; Pattillo, A. L.; Servinski, D.; Kruper, W. R.; Carter, D. D.; Guarr, T. F.; Hickey, D. P. Low Viscosity, High Concentration Pyridinium Anolytes for Organic Nonaqueous Redox Flow Batteries. *ACS Appl. Energy Mater.* **2024**, *7* (18), 7640–7648. https://doi.org/10.1021/acsaem.3c02370.

(28) Mtemeri, L.; Hickey, D. P. Model-Driven Design of Redox Mediators: Quantifying the Impact of Quinone Structure on Bioelectrocatalytic Activity with Glucose Oxidase. *J. Phys. Chem. B* **2023**, *127* (36), 7685–7693. https://doi.org/10.1021/acs.jpcb.3c03740.

(29) Costentin, C.; Louault, C.; Robert, M.; Rogé, V.; Savéant, J. M. Reorganization Energy and Pre-Exponential Factor from Temperature-Dependent Experiments in Electron Transfer Reactions. A Typical Example: The Reduction of Tert-Nitrobutane. *Physical Chemistry Chemical Physics* **2012**, *14* (5), 1581–1584. https://doi.org/10.1039/c2cp23050j.

(30) Rosso, K. M.; Smith, D. M. A.; Dupuis, M. An Ab Initio Model of Electron Transport in Hematite (α-Fe2O3) Basal Planes. *Journal of Chemical Physics* **2003**, *118* (14), 6455–6466. https://doi.org/10.1063/1.1558534.

(31) Wu, Q.; Van Voorhis, T. Direct Calculation of Electron Transfer Parameters through Constrained Density Functional Theory. *Journal of Physical Chemistry A* **2006**, *110* (29), 9212–9218. https://doi.org/10.1021/jp061848y.

(32) Buda, M. On Calculating Reorganization Energies for Electrochemical Reactions Using Density Functional Theory and Continuum Solvation Models. *Electrochim. Acta* **2013**, *113*, 536–549. https://doi.org/10.1016/j.electacta.2013.09.045.

(33) Politzer, P.; Murray, J. S. The Fundamental Nature and Role of the Electrostatic Potential in Atoms and Molecules. *Theoretical Chemistry Accounts: Theory, Computation, and Modeling (Theoretica Chimica Acta)* **2002**, *108* (3), 134–142. https://doi.org/10.1007/s00214-002-0363-9.